



# Strong phase coherence and vortex matter in a fractal system with proximity-induced superconductivity

Teramachi, Nanami ; Nakaaki, Iku ; Hashimoto, Aoi ; Ooi, Shuuichi ; Tachiki, Minoru ; Arisawa, Shunichi ; Seto, Yusuke ; Sakurai, Takahiro...

**(Citation)**

Physical Review B, 108(15):155146

**(Issue Date)**

2023-10-15

**(Resource Type)**

journal article

**(Version)**

Version of Record

**(Rights)**

©2023 American Physical Society

**(URL)**

<https://hdl.handle.net/20.500.14094/0100488923>



# Strong phase coherence and vortex matter in a fractal system with proximity-induced superconductivity

Nanami Teramachi,<sup>1</sup> Iku Nakaaki,<sup>1</sup> Aoi Hashimoto,<sup>1</sup> Shuuichi Ooi<sup>1,2</sup>, Minoru Tachiki<sup>1,2</sup>, Shunichi Arisawa<sup>1,3</sup>, Yusuke Seto<sup>1,4</sup>, Takahiro Sakurai<sup>1,5</sup>, Hitoshi Ohta<sup>1,6</sup>, Jaroslav Valenta<sup>1,2</sup>, Naohito Tsujii<sup>1,2</sup>, Takao Mori<sup>1,2,7</sup> and Takashi Uchino<sup>1</sup>

<sup>1</sup>Department of Chemistry, Graduate School of Science, Kobe University, Nada, Kobe 657–8501, Japan

<sup>2</sup>International Center for Materials Nanoarchitectonics (WPI-MANA), National Institute for Materials Science, Tsukuba, Ibaraki 305-0047, Japan


<sup>3</sup>Research Center for Functional Materials, National Institute for Materials Science, Tsukuba, Ibaraki 305-0047, Japan

<sup>4</sup>Department of Geosciences, Graduate School of Science, Osaka Metropolitan University, Sumiyoshi, Osaka 558–8585, Japan

<sup>5</sup>Center for Support to Research and Education Activities, Kobe University, Nada, Kobe 657–8501, Japan

<sup>6</sup>Molecular Photoscience Research Center, Kobe University, Nada, Kobe 657–8501, Japan

<sup>7</sup>Graduate School of Pure and Applied Sciences, University of Tsukuba, Tsukuba, Ibaraki 305–8577, Japan

 (Received 5 October 2022; revised 29 August 2023; accepted 10 October 2023; published 26 October 2023)

We investigate vortex matter in a proximity-coupled Mg/MgO/MgB<sub>2</sub> nanocomposite with ~30 vol. % of MgB<sub>2</sub> using magneto-optical imaging, scanning superconducting quantum interface device microscopy, and pinning-force analysis. This nanocomposite was prepared by spark plasma sintering (SPS) of the MgO/MgO/MgB<sub>2</sub> mixture powders obtained from a solid-phase reaction between Mg and B<sub>2</sub>O<sub>3</sub> [Uchino *et al.*, *Phys. Rev. B* **101**, 035146 (2020)]. The resulting nanocomposite is characterized by scale-free (or fractal) distributions of MgB<sub>2</sub> components and the atomically clean MgO/MgB<sub>2</sub> interfaces. It is also found that high SPS temperature (1200 °C) is the key to improve the proximity-induced superconducting properties of the Mg/MgO/MgB<sub>2</sub> nanocomposite. This proximity-coupled system acts as a fully phase-coherent superconductor with isotropic pinning and strong superfluid phase stiffness irrespective of the low volume fraction of MgB<sub>2</sub>. Our results demonstrate that in contrast to the case of conventional granular superconductors, the grain boundaries in the present system carry high critical currents and have high vortex-pinning efficiency, implying an excellent phase-coherent capability of the proximity-coupled fractal network.

DOI: [10.1103/PhysRevB.108.155146](https://doi.org/10.1103/PhysRevB.108.155146)

## I. INTRODUCTION

When a normal metal (N) and a superconductor (S) are put in contact, their electronic properties are modified within the range of the coherence length, leading to the superconducting proximity effect [1,2]. Previously, the effect of the proximity effect on the superconducting critical temperature  $T_c$  was intensively investigated using various S/N systems [3,4]. An essential criterion for observing the proximity effect is that the size or thickness of the individual components of the S/N systems should be less than their respective coherence lengths ( $\xi_S$  and  $\xi_N$ ), which is known as the Cooper limit. According to this criterion,  $\xi_S$  is the distance up to which the pair-breaking effect of the Cooper pair operates in the superconducting side, whereas  $\xi_N$  represents the distance in which superconductivity “leaks” into the normal region. Recently, however, anomalously long-range proximity effects extending over a distance far beyond the coherence length have been observed in a variety of S/N/S nanostructures with clean interfaces [5–12], even showing a surprisingly uniform superconducting gap in the N region [5]. These phenomena are in contrast to a quick decay of induced gap observed for a conventional S/N junction [1]. Although the true physical origin of such exotic proximity effects is not known, it is most likely that the Andreev reflection [13,14], which creates phase-coherent electron/hole pairs in the N region, and the related collective phase-coherence

state play a vital role. As for SNS double-sided junctions, for example, Andreev reflections can occur at both interfaces multiple times to result in the coherent charge transport across the junctions [3]. Note also that when a magnetic field is applied to these proximity-induced superconducting regions, quantized vortices, which we here term “proximity vortices,” are supposed to be created [15–21]. Although the vortices in tunnel Josephson junctions are believed to be coreless [15], recent theoretical and experimental investigations have provided evidence that the magnetic flux penetrated in long diffusive S/N/S junctions [18–20] or some grain boundaries [21] is quantized to form proximity vortices containing cores with suppressed gaps. Hence, it is interesting to investigate the nature of flux patterns and the related critical current distributions in these exotic proximity systems. However, no detailed report has been published on such issues, nor on the role of pinning force on the structure and properties of proximity vortices.

In this work, we investigate the superconducting and flux-pinning properties of proximity-coupled superconductors by using a Mg/MgO/MgB<sub>2</sub> fractal nanocomposite with ~30 vol. % MgB<sub>2</sub>, which can be viewed as a fractal assembly of long diffusive SNS junctions near or below the percolation threshold. Recently, we [22] have shown that such a fractal system behaves as a bulk type-II-like superconductor

from electrical, magnetic, and transverse-field muon spin rotation (TF- $\mu$ SR) measurements irrespective of the low volume fraction of superconducting ( $\text{MgB}_2$ ) nanograins, exhibiting anomalously enhanced proximity effect. In this nanocomposite, a large amount of the vortices generated by an applied field are supposed to be proximity vortices. Hence, the present nanocomposite system can be used to explore the nature of proximity vortices and their pinning behavior. We here explore the flux patterns by means of magneto-optical (MO) imaging and scanning superconducting quantum interference device (SQUID) microscope methods. We also analyze the field and temperature dependence of the pinning force on the basis of a scaling law for flux pinning.

## II. EXPERIMENTAL PROCEDURES

The bulk forms of the  $\text{Mg}/\text{MgO}/\text{MgB}_2$  fractal nanocomposites were synthesized by the solid-phase reaction of  $\text{Mg}$  and  $\text{B}_2\text{O}_3$  powders under Ar atmosphere at  $700^\circ\text{C}$ , followed by a subsequent spark plasma sintering (SPS) procedure under vacuum, basically according to the procedure reported in Ref. [22] (for details, see Supplemental Material [23]). The only difference in the sample preparation process between previous and present works is the SPS sintering temperature, which was set to  $650^\circ\text{C}$  in Ref. [22]. In the present work, the sintering temperature was raised to  $1200^\circ\text{C}$  to prepare samples with higher density and better proximity-induced superconducting properties, as will be shown below.

The structural, morphological, electrical, and magnetic properties of the thus obtained  $\text{Mg}/\text{MgO}/\text{MgB}_2$  nanocomposite have been investigated using x-ray diffraction (XRD), field-emission scanning electron microscopy (FESEM), and high-resolution transmission electron microscopy (HR-TEM). The perpendicular component of the magnetic flux density was explored by MO imaging and SQUID microscopy. Details of the measurements are given in Supplemental Material [23].

## III. RESULTS

### A. Basic structural and superconducting properties

From the XRD pattern and the Rietveld pattern fitting, the composition of the nanocomposite obtained by SPS at  $1200^\circ\text{C}$  was found to be  $\text{MgO}$  75.8 wt. %,  $\text{MgB}_2$  23.7 wt. %, and  $\text{Mg}$  0.5 wt. % [Fig. 1(a)], corresponding to the approximate volume fractions of  $\text{MgO}$  69%,  $\text{MgB}_2$  30%, and  $\text{Mg}$  1%. According to the Scherrer equation, the average crystalline sizes of  $\text{MgO}$ ,  $\text{MgB}_2$ , and  $\text{Mg}$  are 42, 40, and 29 nm, respectively. For comparison, we show in Fig. 1(b) the XRD pattern of the sample obtained by SPS at  $650^\circ\text{C}$  reported in our previous paper [22]. The weight fraction of  $\text{Mg}$  ( $\text{MgB}_2$ ) decreases (increases) as the sintering temperature of SPS increases from  $650$  to  $1200^\circ\text{C}$ . We also found that the densification ratio, which is defined as the ratio between the observed bulk density and the ideal density, increases from 79.4 to 96.7% with increasing SPS temperature from  $650$  to  $1200^\circ\text{C}$ . These changes in the composition and density probably result from the fact that as the sintering process proceeds at temperatures higher than  $\sim 1000^\circ\text{C}$ , magnesium

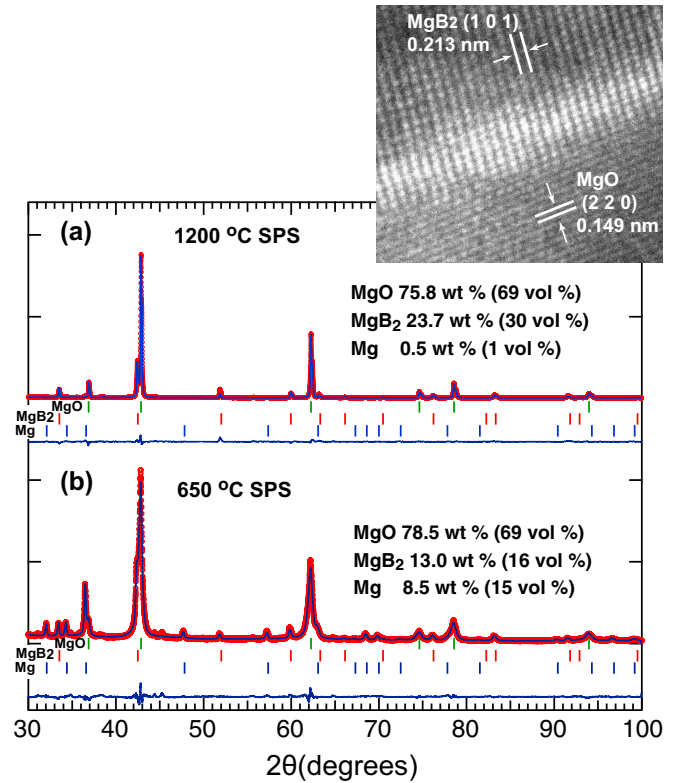


FIG. 1. XRD pattern and output from quantitative Rietveld analysis of (a)  $1200^\circ\text{C}$  SPS sample and (b)  $650^\circ\text{C}$  SPS sample [22]. Lower curve is difference between observed data and calculated intensity at each step, plotted on same scale. Inset in (a) shows typical high-resolution TEM (HR-TEM) image of  $\text{MgO}/\text{MgB}_2$  interface for  $1200^\circ\text{C}$  SPS sample.

is evaporated (the boiling point of magnesium is around  $1090^\circ\text{C}$ ), resulting in a highly dense body of the sintered sample consisting mostly of  $\text{MgO}$  and  $\text{MgB}_2$ . It should be noted, however, that even after SPS at  $1200^\circ\text{C}$ , the interface between the  $\text{MgO}$ - and  $\text{MgB}_2$ -rich regions is still atomically clean and free of defects and voids, as seen in a HR-TEM image [see the inset of Fig. 1(a)]. This clean interface will be essential to induce a robust and long-range proximity effect [5–12]. We then performed elemental mapping on the  $1200^\circ\text{C}$  SPS sample using FESEM/energy-dispersive x-ray spectroscopy (EDX) imaging and scanning transmission electron microscope (STEM)/EDX imaging techniques. The complex nanostructures of the present sample are recognized by FESEM/EDX imaging and STEM/EDX imaging [Fig. 2(a)]. We see hierarchical micro/nanostructures consisting of highly complicated  $\text{MgO}$ -rich domains surrounded by barely interconnected  $\text{MgB}_2$ -rich regions irrespective of magnification. This hierarchical structural complexity across many scales is reminiscent of fractal patterns [24], similar to the case of the  $650^\circ\text{C}$  SPS sample [22]. The fractal dimension of boron estimated from a box-counting method is  $\sim 1.8$  [Fig. 2(b)]. Thus, the fractal distribution of  $\text{MgB}_2$  as well as the clean heterointerface characteristics are retained in the  $1200^\circ\text{C}$  SPS sample.

Figure 3(a) shows the temperature-dependent resistivity of the  $650$  and  $1200^\circ\text{C}$  SPS samples in the temperature

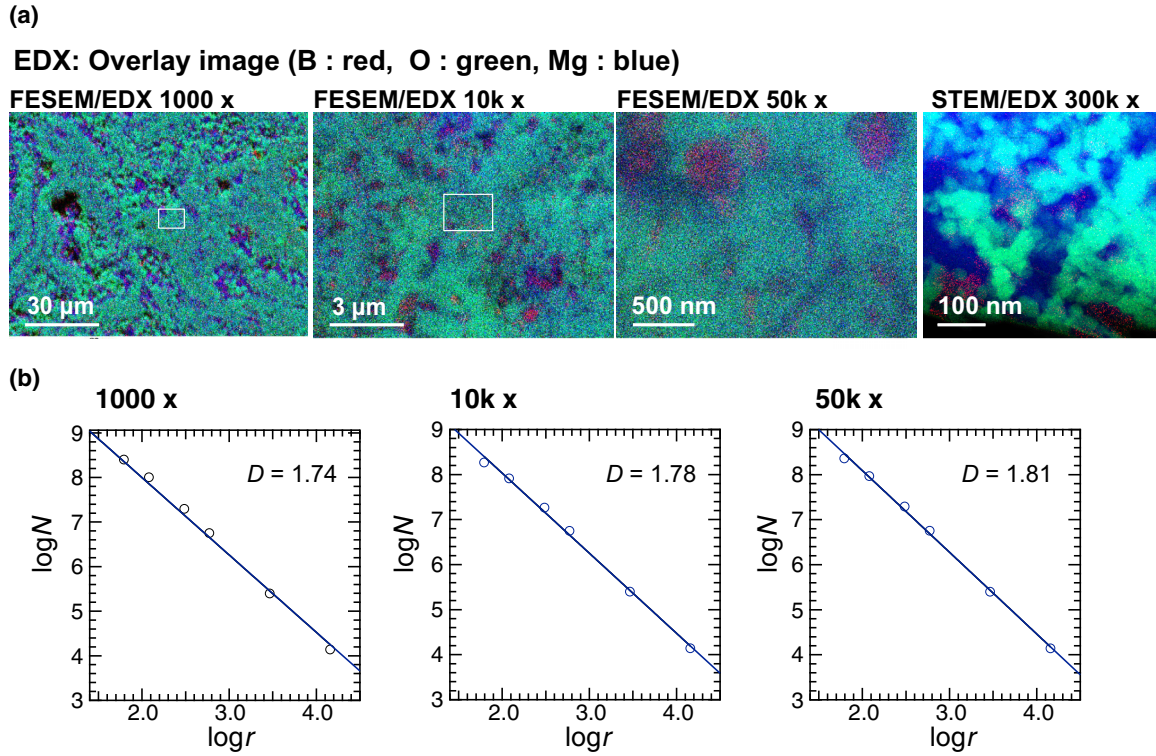


FIG. 2. (a) FESEM/EDX and STEM/EDX overlay images of 1200 °C SPS sample in different magnifications; red = B, green = O, blue = Mg. White box in FESEM/EDX images indicates appropriate location used for next-higher magnification image. (b) Box-counting analysis for boron distribution in FESEM/EDX images shown in (a). Logarithmic plot of  $N$  vs  $r$ , where  $r$  is dimension of voxels and  $N$  is number of voxels containing EDX signal, obtained from FESEM/EDX images with magnifications of 1000 $\times$ , 10 000 $\times$ , and 50 000 $\times$ . Fractal dimension or box-counting dimension  $D = -\log N / \log r$  is obtained from least-square fit to data.

range from 2 to 300 K. The onset of superconductivity is observed at 38.4 K for both the samples, in basic agreement with that observed from single and polycrystalline  $\text{MgB}_2$  [35–44] (see Table I). This result implies that the onset temperature of superconductivity is governed by the intragrain superconducting properties of  $\text{MgB}_2$  and is hardly affected by the proximity effect. In the conventional S/N systems in the Cooper limit,  $T_c$  shows a sudden decrease as  $d_N/d_S$  increases due to the proximity effect, where  $d_N$  and  $d_S$  are the size (or thickness) of the N and S regions, respectively. However, such a decrease in  $T_c$  is not observed for the S/N systems with  $d_S$  much larger than  $\xi_S$  [3,45,46] because the suppression of the supercurrent occurs on the S side with a depth of  $\sim \xi_S$  and is negligible for the system

of  $d_S \gg \xi_S$ . As will be shown below, the coherence length of the 650 and 1200 °C SPS samples are 6.3 and 5.5 nm, respectively (see Table I), which are far smaller than the average crystalline size of  $\text{MgB}_2$  in the nanocomposites ( $\sim 40$  nm). This may account for the observation that the superconducting onset temperature is not decreased by the proximity effect. Although the superconducting onset temperature is almost identical between the 650 and 1200 °C SPS samples, the zero-resistivity temperature increases from  $\sim 33$  to  $\sim 36$  K with increasing SPS temperature. Hence, the proximity-induced superconducting properties are strongly influenced by the structural and interfacial properties of the normal matrix, possibly via the change in the phase-coherence length in the N region. It is probable that the interfacial properties of

TABLE I. Comparison of physical parameters with poly- and single-crystalline  $\text{MgB}_2$ .

	$T_c$ (K)	$\Delta T_c$ (K)	$H_{c1}(0)$ (Oe)	$H_{c2}(0)$ (kOe)	$\xi(0)$ (nm)	$\lambda(0)$ (nm)
650 °C SPS <sup>a</sup>	38.4 <sup>b</sup>	5.0 <sup>b</sup>	96	83.5	6.3	252
1300 °C SPS	38.4 <sup>b</sup>	2.3 <sup>b</sup>	580	110	5.5	89
Poly-crystalline $\text{MgB}_2$	39, <sup>c,f</sup> 37 <sup>d</sup>	1, <sup>c</sup> 0.5 <sup>e</sup>	300, <sup>d</sup> 320 <sup>f</sup>	125 <sup>d,e</sup>	5.2 <sup>e</sup>	140 <sup>e</sup>
Single crystalline $\text{MgB}_2$	38.6, <sup>g</sup> 37.9 <sup>k</sup> 38.8 <sup>l</sup>	0.3 <sup>l</sup>	$\parallel ab$ 220 <sup>i</sup> 450 <sup>j</sup> $\parallel c$ 630, <sup>l</sup> 534 <sup>j</sup>	$\parallel ab$ 198, <sup>g</sup> 136 <sup>h</sup> $\parallel c$ 77 <sup>g,e</sup> 34 <sup>h</sup>	$\parallel ab$ 6.5, <sup>g</sup> 10 <sup>h</sup> $\parallel c$ 2.5, <sup>g</sup> 3 <sup>h</sup>	$\parallel ab$ 76, <sup>j,k</sup> 82 <sup>i</sup> $\parallel c$ 370 <sup>i</sup>

<sup>a</sup>Reference [22]; <sup>b</sup>Obtained from the resistivity measurements; <sup>c</sup>Reference [35]; <sup>d</sup>Reference [36]; <sup>e</sup>Reference [37]; <sup>f</sup>Reference [38]; <sup>g</sup>Reference [39]; <sup>h</sup>Reference [40]; <sup>i</sup>Reference [41]; <sup>j</sup>Reference [42]; <sup>k</sup>Reference [43]; <sup>l</sup>Reference [44].



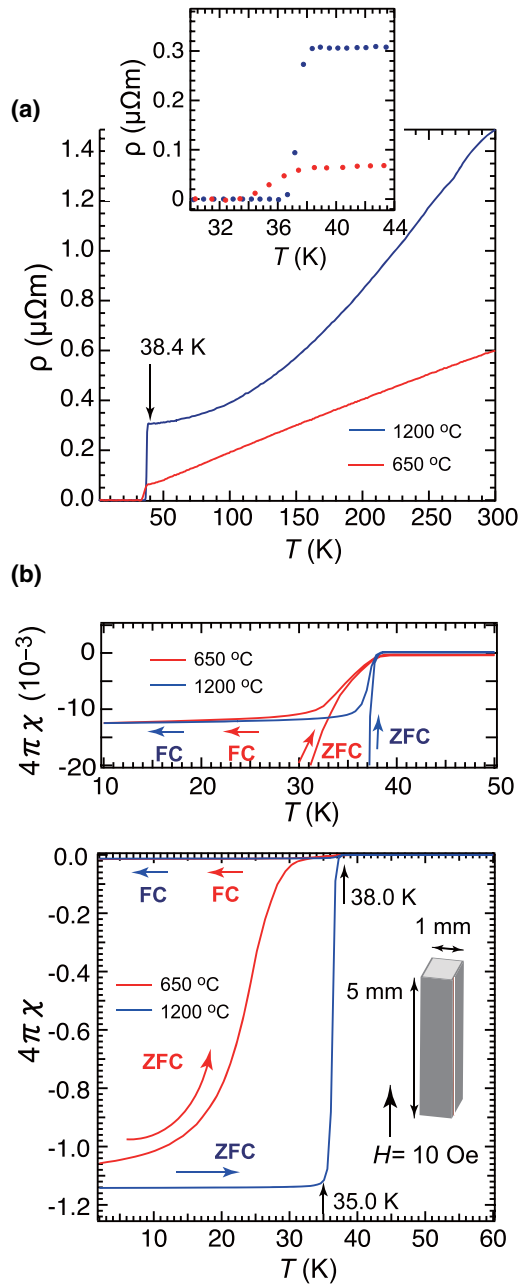


FIG. 3. Comparison of superconducting properties between 650 °C [22] and 1200 °C SPS samples. (a) Temperature-dependent resistivity. (b) Zero-field-cooling (ZFC) and field-cooling (FC) magnetic susceptibility ( $4\pi\chi$ ) curves under applied field of 10 Oe. Upper panel shows magnification of lower panel around transition temperature region. Inset in lower panel shows schematic illustration of cuboid sample used for magnetic measurements. Field was applied along long side of sample to minimize effect of demagnetizing fields (for details, see Methods in the Supplemental Material [23]).

MgO/MgB<sub>2</sub>, rather than those of Mg/MgB<sub>2</sub>, will play a more vital role in inducing the proximity-induced superconductivity since Mg hardly exists in the 1200 °C SPS sample.

In the field-cooling (FC) and zero-field-cooling (ZFC) susceptibility curves [Fig. 3(b)], we also observe a superconducting onset at 38.0 K for both the samples. In the ZFC susceptibility curve of the 1200 °C SPS sample, the value of

$4\pi\chi$  is decreased sharply below the onset temperature and becomes almost constant at temperatures lower than 35.0 K, showing a transition width of  $\Delta T_c = 3$  K. However, the 650 °C SPS sample does not show such a sharp transition but exhibits a gradual decrease in  $4\pi\chi$  with decreasing temperature for both the ZFC and FC curves. Here, we should note that the lowest-temperature ZFC magnetic susceptibility ( $4\pi\chi$ ) of these samples slightly exceeds the ideal value of perfect diamagnetism ( $-1$ ), which may be due to the neglect of the demagnetization correction. In this work, the DC magnetization measurements were carried out for a square cuboid-shape sample with dimensions of  $1 \times 1 \times 5$  mm<sup>3</sup> by applying a magnetic field along the long side of the sample to reduce possible demagnetizing effects [see also the inset of Fig. 3(b)]. In this configuration, the resulting effective demagnetization factor  $D$  is estimated to be  $\sim 0.05$  [25]. This means that when the applied field is 10 Oe, the strength of the internal field is increased to  $\sim 10.5$  Oe. If we perform the demagnetization correction using  $D = 0.05$ , the lowest-temperature values of  $4\pi\chi$  for these samples become more closer to the ideal value of  $-1$ . Hence, it is most likely that a nearly perfect diamagnetism is realized in these nanocomposite at sufficiently low temperatures, as was already demonstrated in our previous TF- $\mu$ SR measurements [22] and will be also shown in the MO observations later. We should also note the FC curves show a very low Meissner fraction ( $< \sim 1\%$ ) for both the samples. These features are not observed in MgB<sub>2</sub> single crystals [39,40] but are often observed in MgB<sub>2</sub> polycrystalline samples with strong pinning [38,47]. The above results indicate that the nanocomposite samples can be regarded as bulk type-II superconductors with strong pinning.

We next explored the initial  $M(H)$  ZFC curves to estimate the temperature dependence of the lower critical fields of the 1200 °C SPS sample [Fig. 4(a)]; the extrapolated value at zero temperature  $H_{c1}(0)$  is estimated to be 580 Oe [see the inset of Fig. 4(a)], which is substantially larger than that obtained for the 650 °C SPS sample ( $H_{c1}(0) = 96$  Oe [22]; see Table I). This indicates that the magnetic flux is more difficult to penetrate into the 1200 °C SPS sample. One also sees from Table I that the  $H_{c1}(0)$  value for the 1200 °C SPS sample is comparable to or even higher than those reported for MgB<sub>2</sub> single crystals [41,42] and polycrystals [36,38]. As will be shown in Sec. III B, the magnetic flux penetrates the 1200 °C SPS sample gradually and homogeneously above  $H_{c1}$  rather than avalanching into it, which is often the case with MgB<sub>2</sub> polycrystals.

The magnetoresistivity measurements were performed to evaluate the upper critical field  $H_{c2}$  of the 1200 °C SPS sample [Fig. 4(b)]. In this work,  $H_{c2}(T)$  was defined as the applied field for which the sample resistance measured at  $T$  is 10% of the normal state value. We found that the  $H_{c2}(T)$  curve shows a positive curvature near  $T_c$ , as also observed in the  $H_{c2}(T)$  curve of the 650 °C SPS sample [22] and MgB<sub>2</sub> polycrystals [36–38] as well as the  $H_{c2}^{||ab}$  curve of MgB<sub>2</sub> single crystals [39,40]. Such a positive curvature of  $H_{c2}(T)$  has also been observed in transition-metal borocarbides [48–51] and has been interpreted in terms of clean-limit type-II superconductors. As reported in Ref. [51], this temperature dependence can be described by the simple expression

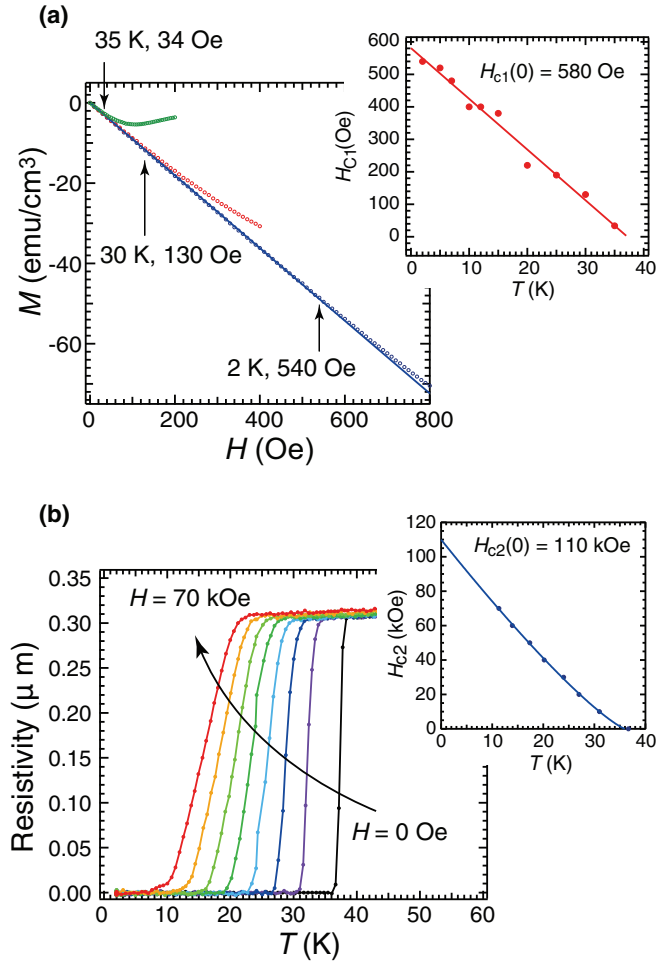


FIG. 4. (a) Initial ZFC  $M(H)$  curves of 1200 °C SPS sample obtained at 2, 30, and 35 K. Black line indicates linear fit in low-field region, showing Meissner line. Point of departure from Meissner line is indicated by arrow, which represents lower critical field  $H_{c1}$ . Inset shows  $H_{c1}$  as function of temperature along with linear fit of data. (b) Resistive superconducting transition in different applied fields (from bottom right to top left) from 0 to 70 kOe in steps of 10 kOe. Inset shows temperature dependence of upper critical field  $H_{c2}$  defined as field for which sample resistance is 10 % of normal state value. Solid line represents fit of function  $H_{c2}(T) = H_{c2}(0)(1 - T/T_c)^{1+\alpha}$ . Fitted values of  $H_{c2}(0)$  and  $\alpha$  are 110.0 kOe and 0.21, respectively.

$H_{c2}(T) = H_{c2}(0)(1 - T/T_c)^{1+\alpha}$  [see the solid line in the inset of Fig. 4(b)]. The parameter  $\alpha > 0$  describing the positive curvature of  $H_{c2}(T)$  characterizes the sample quality and becomes 0 in the case of the dirty limit. The fitted values of  $H_{c2}(0)$  and  $\alpha$  are found to be 110.0 kOe and 0.21, respectively. The fitted  $\alpha$  value is almost comparable to those of the 650 °C SPS sample ( $\alpha = 0.28$ ) [22], MgB<sub>2</sub> polycrystals ( $\alpha = 0.25 - 0.32$ ) [52], and YLu<sub>1-x</sub>Ni<sub>2</sub>B<sub>2</sub>C ( $\alpha = 0.10 - 0.25$ ) [51], implying the absence of impurity scattering in these samples. On the other hand, the  $H_{c2}(0)$  value obtained for the 1200 °C SPS sample is appreciably higher than that reported for the 650 °C SPS sample ( $H_{c2}(0) = 83.5$  kOe [22]; see Table I). Note also that the  $H_{c2}(0)$  value for the 1200 °C SPS sample is similar to that of MgB<sub>2</sub> polycrystals ( $H_{c2}(0) = 125$  kOe [36,37]; see

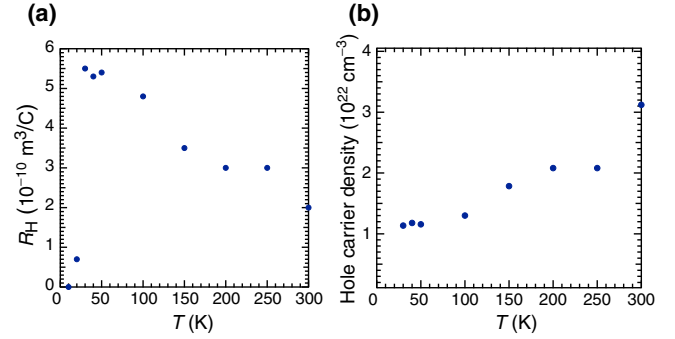


FIG. 5. (a) Temperature dependence of Hall coefficient  $R_H$ . (b) Temperature dependence of hole carrier density calculated from  $1/eR_H$ . Measurements were performed for 1200 °C SPS sample.

Table I) and is slightly smaller than  $H_{c2}^{\parallel ab}(0)$  of MgB<sub>2</sub> single crystals ( $H_{c2}^{\parallel ab}(0) = \sim 140 - \sim 200$  kOe [39–41]; see Table I). This suggests that the coherence length of the vortices in the 1200 °C SPS sample is shorter than that in the 650 °C SPS sample and becomes comparable to that of MgB<sub>2</sub> polycrystals. If we apply the Ginzburg-Landau (GL) theory to the 1200 °C SPS sample and use the lower [ $H_{c1}(0) = 580$  Oe] and upper [ $H_{c2}(0) = 110$  kOe] critical fields, the penetration depth  $\lambda$  and the coherence length  $\xi$  are estimated to be 89 and 5.5 nm, respectively (for details of calculations, see Supplemental Material [23]). The obtained value of  $\xi$  is almost equal to that of MgB<sub>2</sub> polycrystals ( $\xi = 5.2$  nm [37]; see Table I), as expected, and the large GL parameter ( $\kappa = \lambda/\xi \sim 16$ ) calculated for the 1200 °C SPS sample is consistent with the type-II superconducting behavior. However, the  $\lambda$  value is appreciably shorter than that reported for MgB<sub>2</sub> polycrystals ( $\lambda = 140$  nm [37]; see Table I). Since the 1200 °C SPS sample consists of 30 vol. % of MgB<sub>2</sub>, it can be assumed that the MgB<sub>2</sub>-rich regions accommodate 30% of vortices as conventional Abrikosov vortices. This inversely means that 70% of vortices are nucleated in the MgO-rich regions as proximity vortices. A shorter penetration depth can be viewed as a characteristic feature of proximity vortices in the 1200 °C SPS sample, as will also be discussed in Sec. IV.

It is useful to measure the Hall coefficients ( $R_H$ ) of the 1200 °C SPS sample to identify the type of charge carrier and its density in the normal state [Fig. 5(a)]. We found that  $R_H$  is positive and increases with decreasing temperature, followed by a sudden decrease at temperatures below 30 K, as in the case of pure MgB<sub>2</sub> bulk samples [53]. This not only implies that the major carrier is the hole derived possibly from MgB<sub>2</sub> nanograins, but it also elucidates that the MgO-rich regions act as a good conducting matrix, also contributing the realization of the proximity effect at temperatures below  $\sim 38$  K. Although the true mechanism of the conduction of the MgO-rich regions is not clear at present, long-range electron transfer between oxygen-vacancy defects in the MgO-rich regions [54] may play a role of normal conductors in the conduction process. We should also note that at 100 K, the net hole density  $n_p$  is estimated to be  $1.3 \times 10^{22} \text{ cm}^{-3}$  [Fig. 5(b)], which is an order smaller than that of pure MgB<sub>2</sub> ( $n_p \sim 2 \times 10^{23} \text{ cm}^{-3}$  [53]), in harmony with the low volume fraction ( $\sim 30\%$ ) of MgB<sub>2</sub> in the present nanocomposite.

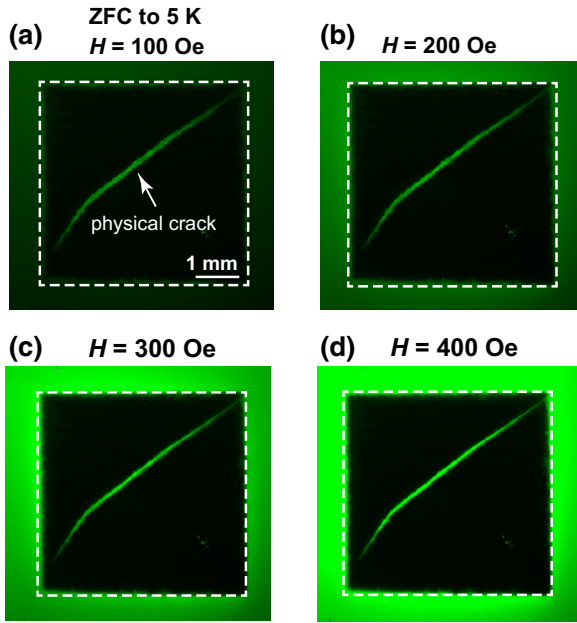


FIG. 6. MO observations after ZFC 1200 °C SPS sample to 5 K and applying magnetic field of (a) 100, (b) 200, (c) 300, and (d) 400 Oe. Edge of sample is indicated by dashed white line.

### B. MO imaging measurements

Using the 1200 °C SPS sample, we performed a series of zero-field-cooled MO measurements on the plate sample with dimensions of  $5 \times 5 \times 1 \text{ mm}^3$  to explore the flux-penetration behavior. In the MO images, the penetration of the flux is imaged as bright areas, whereas the flux-free area stays dark. We found that in agreement with a high  $H_{c1}$  value [ $H_{c1}(0) = 580 \text{ Oe}$ ], magnetic flux hardly penetrates into the sample on applying magnetic field  $H$  up to  $\sim 400 \text{ Oe}$  at temperatures below 10 K except along the diagonal cracking created accidentally during surface polishing (Fig. 6 and Movie S1 in Ref. [23]), demonstrating the achievement of the perfect diamagnetism at such low temperatures. When the temperature is increased to 30 K, magnetic flux penetration from the four edges can be recognized in the present experimental conditions (Fig. 7(a) and Movie S2 in Ref. [23]). A notable feature in this case is a rather smooth flux front [see the upper panel in Fig. 7(a)], unlike the case of ordinary polycrystalline and granular samples into which magnetic flux easily penetrates along the grain boundaries [33,55]. Figure 7(b) shows the flux-density  $B$  profiles at 30 K obtained during the ramp-up stage of  $H$ . The flux gradient is almost constant irrespective of  $H$ , especially for  $H > 280 \text{ Oe}$ , in agreement with the Bean critical-state model [56], yielding the local critical density  $J_c$  of  $1.0 \times 10^4 \text{ A/cm}^2$  from the flux gradient ( $\mu_0 J_c = dB/dx$ ). This value agrees well with that obtained from the magnetization measurements at 30 K, as will be shown later. Smooth flux fronts are also recognized in the MO images during the ramp-up and ramp-down stages of  $H$  in the temperature range up to 35 K (Movies S3 and S4 in Ref. [23]). However, when the temperature is set to 36 K or above, the flux density becomes almost comparable to the applied field over the whole surface (Fig. 7(c) and Movies S5 and S6 in Ref. [23]). This not only indicates that at 36 K the proximity-induced

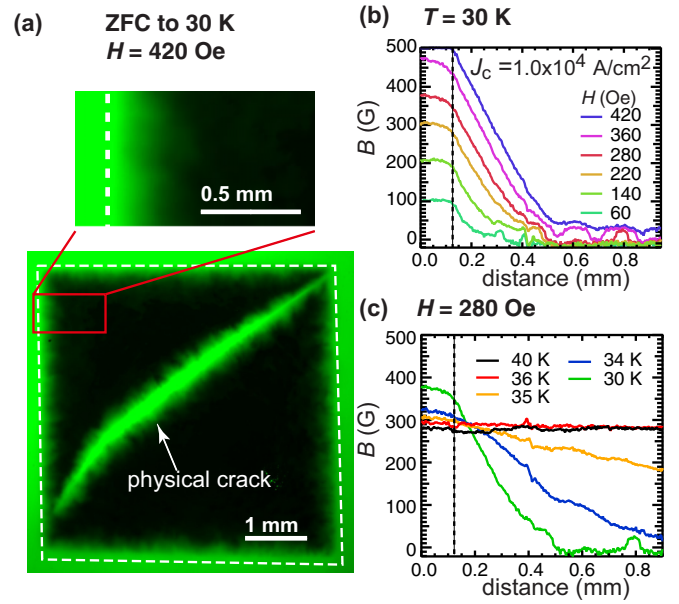


FIG. 7. MO observations after ZFC of 1200 °C SPS sample. (a) MO image of sample ZFC to 30 K and applying magnetic field of 420 Oe. Edge of sample is indicated by dashed white line. Upper panel shows enlarged image of red box region. (b) Typical profiles of flux density at 30 K near edge of sample with increasing  $H$  from 0 to 420 Oe. (c) Temperature dependence of flux-density profiles observed in applied field of 280 Oe. In (b) and (c), dashed vertical line indicates sample edge. Flux density near sample edge exceeds applied field due to demagnetizing effect.

$J_c$  becomes virtually zero, but it also demonstrates that the constituent  $\text{MgB}_2$  grains, which are supposed to be still in the superconducting state at such temperatures, cannot effectively pin the vortices.

We next carried out the MO observations after field cooling in  $H$  of 100 Oe to 30 K in the central area ( $135 \times 135 \mu\text{m}^2$ ) of the sample, where the effect of sample edge is supposed to be neglected. Figure 8(a) demonstrates the resulting MO image, showing a rather homogeneous perpendicular flux distribution  $B_z$  of  $\sim 100 \text{ G}$  [see also the inset of Fig. 8(a)]. Note, however, that such a homogeneous flux distribution of  $\sim 100 \text{ G}$  is almost retained even after switching off the field [Fig. 8(b)]. This allows us to confirm that the vortices are strongly pinned over the whole area of the sample. In other words, large enough normal regions become superconducting due to the proximity-induced superconductivity, leading to sufficiently strong pinning forces throughout the whole area of the sample. Since  $B_z$  obtained from a thick-plate sample is generated mainly by the sum of a two-dimensional vortex current flow in the near-surface region [33], a numerical inversion of Biot-Savart law can provide a map of the semi-quantitative current distribution in the sample surface [32] (for details, see Supplemental Material [23]). Figures 8(c) and 8(d) show a mapping of the corresponding current vectors calculated by using the MO image shown in Figs. 8(a) and 9(b). In the FC state, no net current flows through the sample [Fig. 8(c)], meaning that all the local vortex currents virtually cancel out due to the high homogeneity in the flux distribution. In the remanent state, however, there exists the



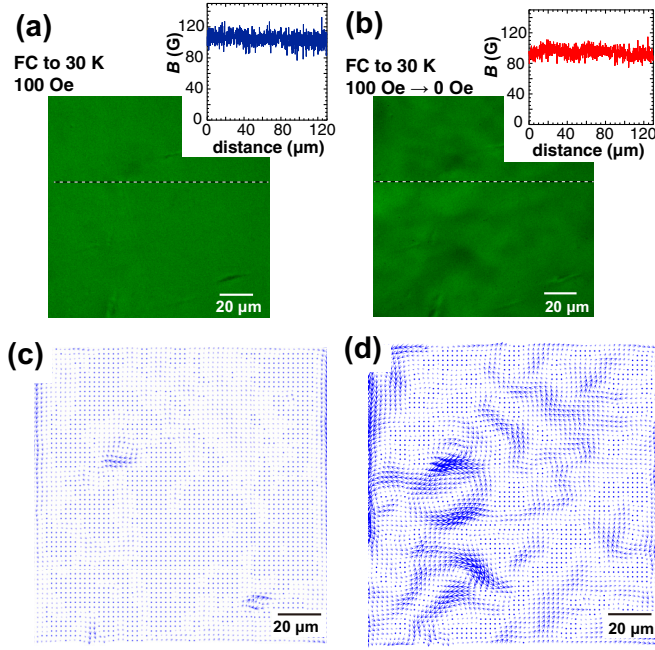


FIG. 8. MO images of 1200°C SPS sample in central area ( $135 \times 135 \mu\text{m}^2$ ) of sample after (a) FC to 30 K in applied field of 100 Oe and (b) subsequent switching off field. Insets in (a), (b) show flux-density profiles along white dashed line in respective MO images. Current distribution patterns calculated by using MO image shown in (a) and (b) are given in (c) and (d), respectively. Arrow length represents magnitude of absolute current density.

region where the current flows continuously and windingly through the surface [Fig. 8(d)]. This indicates that the local circulating vortex currents do not completely cancel out due to the random and irregular distribution of the pinned vortices. It is probable that the resulting critical current density in the proximity-induced superconducting regions is so high to induce the long-range current flow whole through the sample, which is consistent with a bulk type-II-like superconducting behavior.

### C. Scanning SQUID microscopy imaging measurements

In a type-II superconductor, magnetic flux is quantized in units of flux quantum  $\Phi_0$ . It is hence interesting to investigate whether the magnetic flux trapped in the present nanocomposite is quantized or not. In order to clarify the issue, we observed scanning SQUID microscopy (SSM) images of the 1200°C sample field cooled to 3 K in 5 mOe, as shown in Fig. 9(a). The observed SSM image reveals random distributions of bright dots with high magnetic flux density. Also, we found that each bright dot has a magnetic flux  $\Phi$  corresponding to 1 flux quantum  $\Phi_0$  within the uncertainty of the measurement system, which was confirmed by integrating the observed  $B_z$  values around the dot (see Fig. S1 in Ref. [23]). Similar to the case of the MO images mentioned earlier, we can evaluate the local current distribution from the SSM image using a numerical inversion scheme of Biot-Savart law. It should be noted, however, that the calculated current distribution does not correspond to the real spatial scale of the vortex current because of the limited spatial resolution (typically a

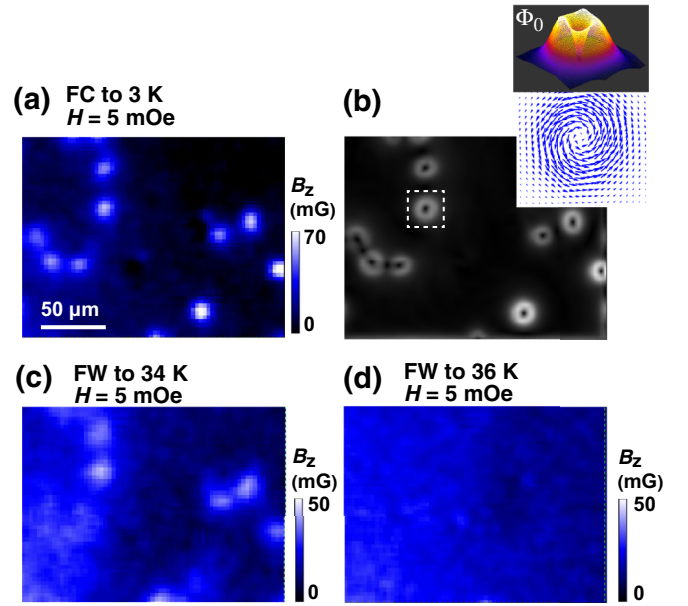


FIG. 9. (a) Scanning SQUID microscope (SSM) image of 1200°C SPS sample taken after FC to 3 K in 5 mOe. (b) Super-currents calculated from SSM image shown in (a). Insets represent local current distribution of white box region in forms of 3D false color image (upper inset) and current vectors (lower inset). Images (c), (d) show SSM images taken after field warming (FW) to (c) 34 K and (d) 35 K in 5 mOe.

few micrometers) of the SSM technique [57,58]. The spatial resolution is limited by the size of the pickup loop (10  $\mu\text{m}$ ), and by the distance between the pickup loop and the sample (about 5  $\mu\text{m}$ ). Consequently, the images represent the perpendicular magnetic field a few micrometers above the surface of the sample convoluted with the geometry of the pickup loop, resulting in the spatial resolution of a few micrometers. We therefore show the current distribution in Fig. 9(b) just for a qualitative morphological description of the vortex current derived from the MO image shown in Fig. 9(a). One can recognize typical features of a vortex structure, i.e., a central current-free region and its surrounding circulating current [see the insets of Fig. 9(b)]. After measuring the SSM image shown in Fig. 9(a), we then field warmed the sample to 36 K, keeping the applied field at 5 mOe. The resulting temperature-dependent SSM images are given in Figs. 9(c) and 9(d). Although the border of the bright dots becomes blurred with increasing temperature, the dot pattern is still preserved at temperatures up to 34 K [Fig. 9(c)]. When the temperature reaches 36 K, however, the dot signature is erased and is replaced with a nearly homogeneous pattern [Fig. 9(d)]. This observation is fully consistent with the temperature-dependent change in the MO images mentioned earlier. Hence, the bright dots shown in Fig. 9(a) can be regarded as proximity-induced quantized vortices that are pinned randomly in the N regions.

### D. Pinning-force analysis

To get further insight into the origin of the pinning, we performed the pinning-force analysis of the 1200°C sample using the critical current density  $J_c$  derived from the



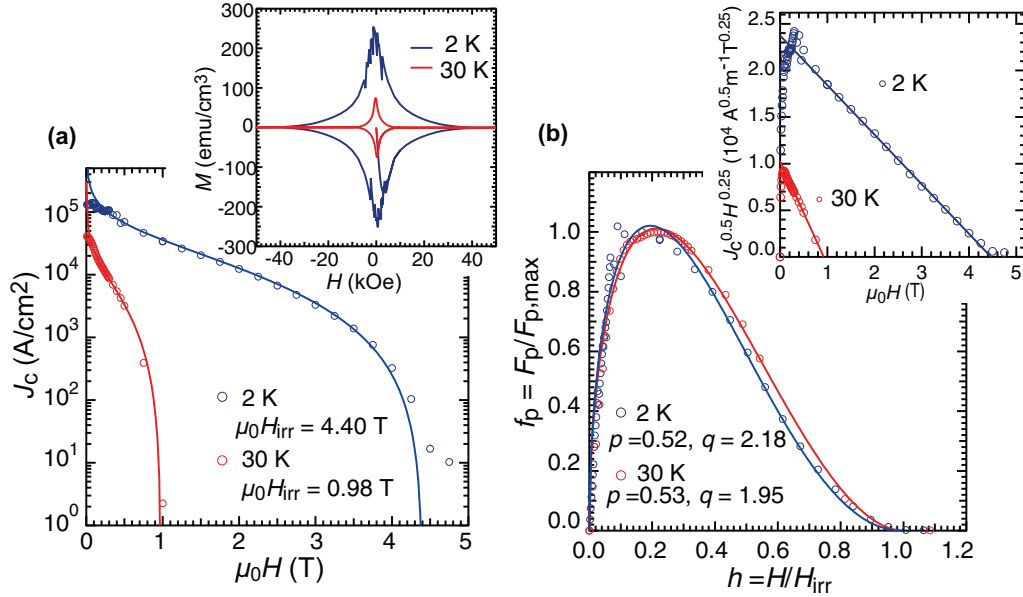


FIG. 10. (a) Critical current density  $J_c$  of 1200 °C SPS sample measured at 2 and 30 K obtained from corresponding  $M(H)$  hysteresis loops given in inset. Solid lines are fits of data to Eq. (1), showing fitted values of  $\mu_0 H_{irr}$ . (b) Normalized pinning-force  $f_p$  curves at 2 and 30 K. Lines are fits to power law  $f_p \propto h^p(1-h)^q$ . Inset demonstrates Kramer plots,  $J_c^{0.5} H^{0.25}$  vs  $\mu_0 H$ .

height of the magnetization loop  $\Delta M$  [inset of Fig. 10(a)] on the basis of the Bean model [51] (for details see the Supplemental Material [23]). The  $J_c$  values in zero magnetic field are  $\sim 1 \times 10^5$  and  $\sim 3 \times 10^4$  A/cm<sup>2</sup> at 2 and 30 K, respectively [Fig. 10(a)]; the latter value is in reasonable agreement with that obtained from the MO images shown in Fig. 7(b). We also found that similar to pure MgB<sub>2</sub> samples, the field dependence of  $J_c$  is well fitted with the following equation:  $J_c \propto [1 - H/H_{irr}]^2 / \sqrt{H H_{irr}}$ , where  $H_{irr}$  is a fitting constant and also represents the field at which  $J_c \rightarrow 0$ , i.e., an irreversibility field [55,59,60]. This equation was originally developed for isotropic superconductors in which a dominant pinning mechanism is grain-boundary pinning [61]. We also found that the reduced pinning force  $f_p = F_p/F_{p,max}$  almost obeys a scaling law of  $f_p \propto h^{0.5}(1-h)^2$ , where  $F_p = \mu_0 H J_c$ ,  $F_{p,max}$  is the maximum pinning force, and  $h$  is the reduced field  $h = H/H_{irr}$ , as shown in Fig. 10(b). This scaling behavior with  $p \approx 0.5$  and  $q \approx 2$  along with a well-defined linear behavior of the Kramer plot [ $J_c^{0.5} H^{0.25}$  vs  $\mu_0 H$ ; see the inset of Fig. 10(b)] allows us to confirm that the isotropic pinning due to grain boundaries is the main cause of pinning as in the case of pure polycrystalline MgB<sub>2</sub> samples where grain boundaries do not limit the current flow [55]. This result is consistent with the long-range current flow across the grains shown in Fig. 8(d).

#### IV. DISCUSSION

In the conventional MgB<sub>2</sub> composites, heteroboundaries behave as weak links with substantially lower critical currents, deteriorating a global superconducting phase coherence as the volume fraction of MgB<sub>2</sub> decreases below  $\sim 50\%$  [62,63]. Hence, it is likely that in the present nanocomposite, the hierarchically constructed structures and the clean MgO/MgB<sub>2</sub> interfaces induce an anomalously long-range proximity effect

within the fractally connected Josephson network, leading to the observed global-phase coherence. We suggest that the solid-phase reaction between Mg and B<sub>2</sub>O<sub>3</sub> plays a vital role in creating the fractal and self-organizing morphology with clean MgO/MgB<sub>2</sub> interfaces [22]. In order to confirm this, we prepared the Mg/MgO/MgB<sub>2</sub> nanocomposite having similar compositions with the fractal nanocomposite by SPS of a simple mixture of commercial Mg, MgO, and MgB<sub>2</sub> powders [Fig. 11(a)] and investigated its structural and superconducting properties. We found that the resulting bulk composite does not have a self-similar structure, but rather consists simply of MgB<sub>2</sub>-rich and deficient regions [Fig. 11(b)]. Also, this simple mixture composite has a lower zero-resistivity temperature (Fig. 12), imperfect magnetic shielding [Fig. 13(a)], and weaker vortex pinning [Fig. 13(b)] as compared with the fractal nanocomposite. It is probable that the proximity-induced superconducting regions are developed in some parts of the simple mixture composite as the sample shows zero resistivity at  $\sim 34$  K and a gradual decrease in the ZFC magnetic susceptibility at temperatures below 20 K. However, the degree of phase coherence is imperfect and is much lower than that realized in the fractal nanocomposite. These results support our arguments that the strong global-phase coherence is realized in the present nanocomposite with complex and self-organizing structures with atomically clean interfaces.

In considering the origin of the global-phase coherence, it is interesting to compare the results between the 650 to 1200 °C SPS samples. As noted earlier, the  $\lambda(0)$  value of the 1200 °C value is substantially shorter than that of the 650 °C SPS sample. We should note that  $\lambda(0)$  is a good measure of the superfluid phase stiffness  $J_s$  [64–68], i.e., the energy associated with the phase rigidity of the superconducting coherence. In Josephson coupled systems and/or superconductors with small superfluid density,  $J_s$  becomes lower than the superconducting energy gap  $\Delta$ , and, accordingly, the value of  $T_c$  as

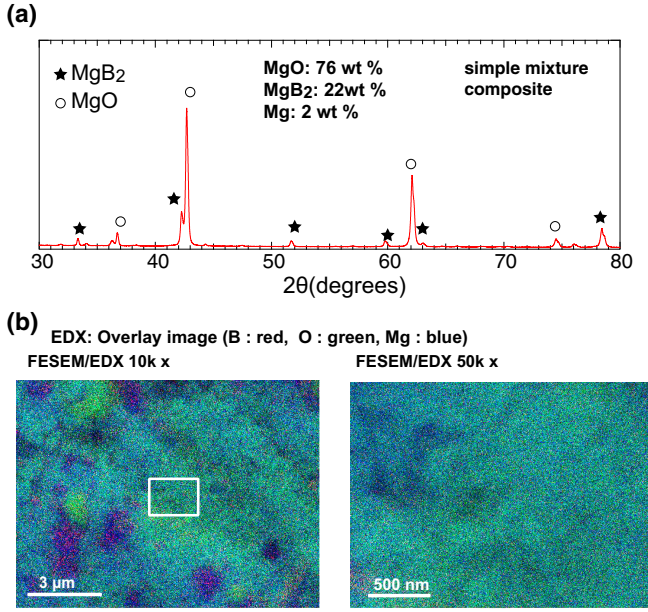


FIG. 11. (a) XRD patterns of simple mixture composite prepared by same SPS condition as that of 1200 °C SPS sample using appropriate mixture of commercial Mg, MgO, and MgB<sub>2</sub> powders. Molar ratio of Mg/MgO/MgB<sub>2</sub> in starting mixture powder was so controlled as to yield similar composition to that of fractal nanocomposite. Results of Rietveld quantitative analysis are shown. (b) FESEM/EDX overlay images of simple mixture composite in different magnifications; red = B, green = O, blue = Mg. White box in left image indicates appropriate location used for higher-magnification image shown in right panel.

well as its systematic variation from one material to another is controlled by  $J_s$  [64–68]. Similarly, the proximity-induced superconducting transition in our samples is also expected to be phase driven, due to the large volume fraction of the normal regions. Now,  $J_s$  can be defined by [26,65]

$$J_s = \frac{\hbar^2 a n_s(0)}{4m^*} = \frac{(\hbar c)^2 a}{16\pi [e\lambda(0)]^2}, \quad (1)$$

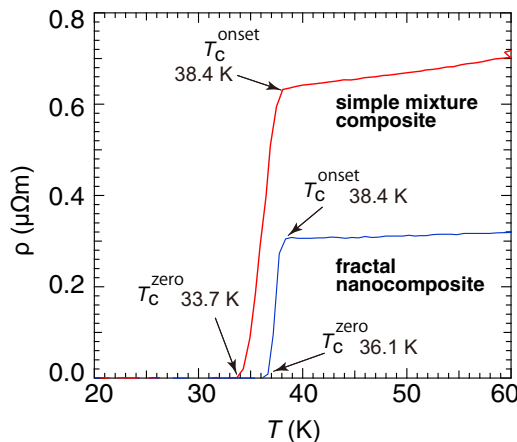


FIG. 12. Comparison of resistivity between 1200 °C SPS sample (fractal nanocomposite) and simple mixture composite.

where  $a$  is the length scale over which the phase fluctuates,  $m^*$  is the effective mass of the electron,  $e$  is the electronic charge, and  $n_s$  is the superfluid density given by

$$n_s(0) = \frac{m^* c^2}{4\pi [e\lambda(0)]^2}. \quad (2)$$

Hence,  $J_s$  is inversely proportional to the square of  $\lambda(0)$ . One sees from Table I that the estimated value of  $\lambda(0)$  decreases from 252 to 92 nm as the SPS temperature increases from 650 to 1200 °C. This decrease in the value of  $\lambda(0)$  implies that the phase of the global order parameter becomes stiffer and the phase fluctuations attempting to destroy the long-range phase correlation are suppressed. The above argument is consistent with the fact that the superconducting properties of the 1200 °C SPS sample are more robust against temperature and applied fields than those of the 650 °C SPS sample. Hence, it is most likely that in the present superconducting nanocomposites,  $J_s$ , rather than  $\Delta$ , determines the ability to carry a supercurrent and the related vortex properties.

If this is the case, the natural question arises: where does this strong phase stiffness come from? Unfortunately, we do not have an exact answer to the above question at the moment. However, we should note that randomness or disorder may enhance superconducting correlations under some circumstances [69,70], especially in systems with fractal [71–73] or multifractal [74,75] (i.e., a mixture of monofractals) characteristics. Moreover, scale-free fractal networks can induce an enhanced positive feedback mechanism, leading to strong correlation, self-organization, and network robustness [76,77]. Hence, one possible scenario for the origin of the strong phase stiffness in the present nanocomposite is the formation of a hierarchical network consisting of a number of closed Andreev trajectories, in which the total phase shift is zero or a multiple of  $2\pi$ . That is, the present system can be regarded as a fractal assembly of Andreev loops, leading to a strong macroscopic phase coherence throughout the sample. In such a multi-Josephson-junction loop system, flux quantization can be monitored by using a modulated-field microwave absorption method [78,79], resulting in the trains of absorption peaks. The spacing of the lines in the spectra is determined by a macroscopic flux quantization, which proves the presence of superconducting current loops. Further work is now ongoing to confirm or disconfirm the observation of periodic microwave absorption in our nanocomposite systems.

## V. CONCLUSIONS

We prepared the bulk forms of the Mg/MgO/MgB<sub>2</sub> fractal nanocomposites by the solid-phase reaction of Mg and B<sub>2</sub>O<sub>3</sub> powders under Ar atmosphere at 700 °C, followed by a SPS procedure at 1200 °C. The composition of the nanocomposite was found to be MgO 75.8 wt. %, MgB<sub>2</sub> 23.7 wt. %, and Mg 0.5 wt. %. The thus-prepared nanocomposite is characterized by fractal micro/nanostructures consisting of highly complicated MgO-rich domains surrounded by barely interconnected MgB<sub>2</sub>-rich regions, also showing atomically clean MgO/MgB<sub>2</sub> interfaces. We have shown from the MO observations and the pinning-force analysis that the present

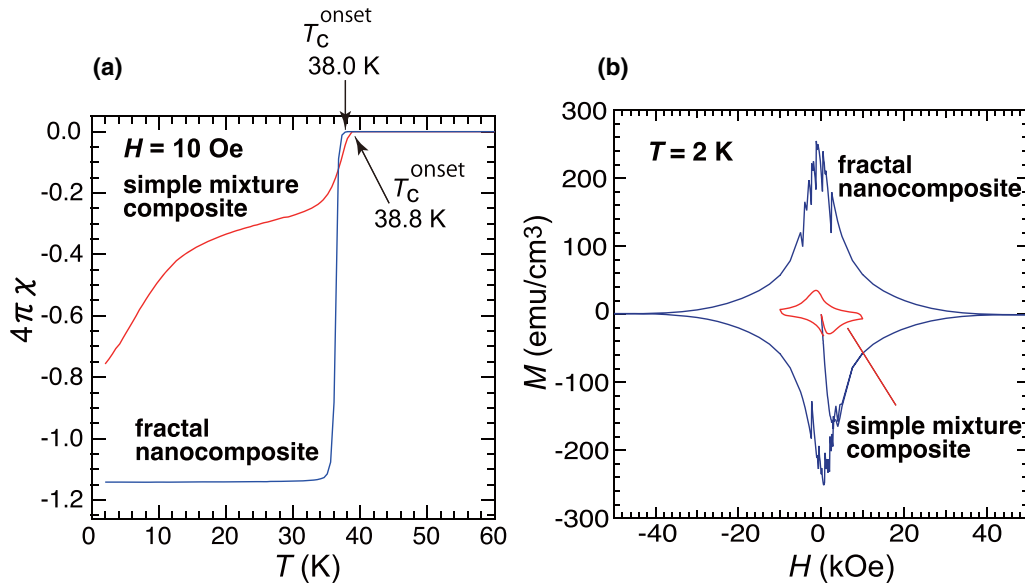


FIG.13. Comparison of superconducting properties of 1200 °C SPS sample (fractal nanocomposite, blue lines) and simple mixture composite (red lines). (a) ZFC magnetic susceptibility ( $4\pi\chi$ ) curves under applied field of 10 Oe, and (b)  $M(H)$  loops at 2 K.

fractal nanocomposite behaves as if it were an isotropic type-II superconductor in terms of magnetic flux expulsion, penetration, and pinning irrespective of the low volume fraction of  $\text{MgB}_2$ . Also, the SSM images have elucidated that proximity-induced quantized vortices are pinned randomly in the  $N$  regions. These results demonstrate that the grain boundaries carry high critical currents and have excellent vortex pinning efficiency, resulting in the establishment of the strong and global-phase coherence throughout the sample. A substantially short penetration depth of 89 nm is predicted for the present sample. This can be interpreted in terms of the generation of the rigid superfluid phase stiffness. Our results not only challenge our conventional understanding of granular superconductors whose transport critical density and pinning strength are limited by weak intergrain coupling, but also imply a high phase-coherence capability of hierarchically coupled proximity network.

#### ACKNOWLEDGMENTS

A part of this work was conducted at Institute for Molecular Science, supported by Nanotechnology Platform Program “Molecule and Material Synthesis” (Grants No. JPMXP09S19MS1063b and No. JPMXP09S20MS1025) of the Ministry of Education, Culture, Sports, Science and Technology (MEXT), Japan. Spark plasma sintering was performed at Fuji Electronic Ind. Co., LTD., Saitama, Japan. Transport measurements were performed by using a Physical Property Measurement System (PPMS) at the CROSS user laboratories. We are indebted to H. Murakami, Osaka University, for providing us a MO plate. T.M. is grateful for support from JST Mirai Grant No. JPMJMI19A1. T.U. acknowledges financial support from a Grant-in-Aid for Scientific Research (Grant No. 21H01622) from the Japan Society for the Promotion of Science (JSPS), the Mitsubishi Foundation, and the Iketani Science and Technology Foundation.

- [1] P. G. de Gennes, Boundary effects in superconductors, *Rev. Mod. Phys.* **36**, 225 (1964).
- [2] K. K. Likharev, Superconducting weak links, *Rev. Mod. Phys.* **51**, 101 (1979).
- [3] J. J. Hauser, H. C. Theuerer, and N. R. Werthamer, Superconductivity in Cu and Pt by means of superimposed films with lead, *Phys. Rev.* **136**, A637 (1964).
- [4] O. Bourgeois, A. Frydman, and R. C. Dynes, Proximity effect in ultrathin Pb/Ag multilayers within the Cooper limit, *Phys. Rev. B* **68**, 092509 (2003).
- [5] J. Kim, V. Chua, G. A. Fiete, H. Nam, A. H. MacDonald, and C.-K. Shih, Visualization of geometric influences on proximity effects in heterogeneous superconductor thin films, *Nat. Phys.* **8**, 464 (2012).
- [6] P. Zareapour, A. Hayat, S. Y. F. Zhao, M. Kreshchuk, A. Jain, D. C. Kwok, N. Lee, S.-W. Cheong, Z. Xu, A. Yang, G. D. Gu, S. Jia, R. J. Cava, and K. S. Burch, Proximity-induced high-temperature superconductivity in the topological insulators  $\text{Bi}_2\text{Se}_3$  and  $\text{Bi}_2\text{Te}_3$ , *Nat. Commun.* **3**, 1056 (2012).
- [7] L. Serrier-Garcia, J. C. Cuevas, T. Cren, C. Brun, V. Cherkez, F. Debontridder, D. Fokin, F. S. Bergeret, and D. Roditchev, Scanning tunneling spectroscopy study of the proximity effect in a disordered two-dimensional metal, *Phys. Rev. Lett.* **110**, 157003 (2013).
- [8] H. Courtois, P. Gandit, D. Mailly, and B. Pannetier, Long-range coherence in a mesoscopic metal near a superconducting interface, *Phys. Rev. Lett.* **76**, 130 (1996).

- [9] A. Yu. Kasumov, O. V. Kononenko, V. N. Matveev, T. B. Borsenko, V. A. Tulin, E. E. Vdovin, and I. I. Khodos, Anomalous proximity effect in the Nb-BiSb-Nb junctions, *Phys. Rev. Lett.* **77**, 3029 (1996).
- [10] S.-G. Jung, D. Pham, T.-H. Park, H.-Y. Choi, J. W. Seo, W. N. Kang, and T. Park, Giant proximity effect in single-crystalline  $\text{MgB}_2$  bilayers, *Sci. Rep.* **9**, 3315 (2019).
- [11] C. Huang, E. Zhang, Y. Liu, X. Yan, J. Wang, C. Zhang, W. Wang, T. Zhou, C. Yi, S. Liu, J. Ling, H. Zhang, R. Liu, R. Sankar, F. Chou, Y. Wang, Y. Shi, Kam T. Law, S. Sanvito, P. Zhou, Z. Han, and F. Xiu, Inducing strong superconductivity in  $\text{WTe}_2$  by a proximity effect, *ACS Nano* **12**, 7185 (2018).
- [12] R.-F. Wang, Y.-L. Xiong, Q. Zhu, M.-Q. Ren, H. Yan, C.-L. Song, X.-C. Ma, and Q.-K. Xue, Anomalous superconducting proximity effect of planar  $\text{Pb} - \text{RhPb}_2$  heterojunctions in the clean limit, *npj Quant. Mater.* **7**, 116 (2022).
- [13] B. Pannetier and H. Courtois, Andreev reflection and proximity effect, *J. Low Temp. Phys.* **118**, 599 (2000).
- [14] T. M. Klapwijk, Proximity effect from an Andreev perspective, *J. Supercond.* **17**, 593 (2004).
- [15] J. R. Clem and M. W. Coffey, Viscous flux motion in a Josephson-coupled layer model of high- $T_c$  superconductors, *Phys. Rev. B* **42**, 6209 (1990).
- [16] J. C. Cuevas, R. Roditchev, T. Chen, and C. Brun, Proximity effect, in *The Oxford Handbook of Small Superconductors*, edited by A. V. Narlikar (Oxford University Press, Oxford, 2017), pp. 108–143.
- [17] V. V. Dremov, S. Yu. Grebenchuk, A. G. Shishkin, D. S. Baranov, R. A. Hovhannissyan, O. V. Skryabina, N. Lebedev, I. A. Golovchanskiy, V. I. Chichkov, C. Brun, T. Cren, V. M. Krasnov, A. A. Golubov, D. Roditchev, and V. S. Stolyarov, Local Josephson vortex generation and manipulation with a magnetic force microscope, *Nat. Commun.* **10**, 4009 (2019).
- [18] D. Roditchev, C. Brun, L. Serrier-Garcia, J. C. Cuevas, V. H. L. Bessa, M. V. Milošević, F. Debontridder, V. Stolyarov, and T. Cren, Direct observation of Josephson vortex cores, *Nat. Phys.* **11**, 332 (2015).
- [19] J. C. Cuevas and F. S. Bergeret, Magnetic interference patterns and vortices in diffusive SNS junctions, *Phys. Rev. Lett.* **99**, 217002 (2007).
- [20] V. S. Stolyarov, T. Cren, C. Brun, I. A. Golovchanskiy, O. V. Skryabina, D. I. Kasatonov, M. M. Khapaev, M. Yu. Kupriyanov, A. A. Golubov, and R. Dimitri, Expansion of a superconducting vortex core into a diffusive metal, *Nat. Commun.* **9**, 2277 (2018).
- [21] H. Hilgenkamp, Ariando, H.-J. H. Smilde, D. H. A. Blank, G. Rijnders, H. Rogalla, J. R. Kirtley, and C. T. Chang, Ordering and manipulation of the magnetic moments in large-scale superconducting  $\pi$ -loop arrays, *Nature (London)* **422**, 50 (2003).
- [22] T. Uchino, N. Teramachi, R. Matsuzaki, E. Tsushima, S. Fujii, Y. Seto, K. Takahashi, T. Mori, Y. Adachi, Y. Nagashima, Y. Sakaguchi, K. Ohishi, A. Koda, T. Sakurai, and H. Ohta, Proximity coupling of superconducting nanograins with fractal distributions, *Phys. Rev. B* **101**, 035146 (2020).
- [23] See Supplemental Material at <http://link.aps.org/supplemental/10.1103/PhysRevB.108.155146> for further details of the sample preparation, additional experimental data, the calculation procedure of local current distribution based on an inverse Biot-Savart procedure, and videos showing the MO images taken during the field ramp-up and ramp-down processes at different temperatures, which includes Refs. [24–34].
- [24] M. Schroeder, *Fractals, Chaos, Power Laws: Minutes from an Infinite Paradise* (Freeman, New York, 1991).
- [25] F. M. Araujo-Moreira, C. Navau, and A. Sanchez, Meissner state in finite superconducting cylinders with uniform applied magnetic field, *Phys. Rev. B* **61**, 634 (2000).
- [26] M. Tinkham, *Introduction to Superconductivity*, 2nd ed. (Dover, New York, 1996).
- [27] S. Ooi, M. Tachiki, T. Konomi, T. Kubo, A. Kikuchi, S. Arisawa, H. Ito, and K. Umemori, Observation of intermediate mixed state in high-purity cavity-grade Nb by magneto-optical imaging, *Phys. Rev. B* **104**, 064504 (2021).
- [28] I. Iguchi, S. Arisawa, K.-S. Yun, and T. Hatano, Direct observation of quantized interlayer vortex flow in a high- $T_c$   $\text{La}_{1.87}\text{Sr}_{0.13}\text{CuO}_4$  single crystal, *Appl. Phys. Lett.* **91**, 202511 (2007).
- [29] T. H. Johansen, M. Baziljevich, H. Bratsberg, Y. Galperin, P. E. Lindelof, Y. Shen, and P. Vase, Direct observation of the current distribution in thin superconducting strips using magneto-optic imaging, *Phys. Rev. B* **54**, 16264 (1996).
- [30] B. J. Roth, N. G. Sepulveda, and P. J. Wikswo, Jr., Using a magnetometer to image a two-dimensional current distribution, *J. Appl. Phys.* **65**, 361 (1989).
- [31] Ch. Jooss, R. Warthmann, A. Forkl, and H. Kronmüller, High-resolution magneto-optical imaging of critical currents in  $\text{YBa}_2\text{Cu}_3\text{O}_{7-\delta}$  thin films, *Physica C* **299**, 215 (1998).
- [32] J. W. Zuber, F. S. Wells, S. A. Fedoseev, T. H. Johansen, A. B. Rosenfeld, and A. V. Pan, A new approach to the inverse problem for current mapping in thin-film superconductors, *J. Appl. Phys.* **123**, 123906 (2018).
- [33] Ch. Jooss, J. Albrecht, H. Kuhn, S. Leonhardt, and H. Kronmüller, Magneto-optical studies of current distributions in high- $T_c$  superconductors, *Rep. Prog. Phys.* **65**, 651 (2002).
- [34] J. Albrecht, Ch. Jooss, R. Warthmann, A. Forkl, and H. Kronmüller, Observation of microscopic currents in superconducting ceramics, *Phys. Rev. B* **57**, 10332 (1998).
- [35] J. Nagamatsu, N. Nakagawa, T. Muranaka, Y. Zenitani, and J. Akimitsu, Superconductivity at 39 K in magnesium diboride, *Nature (London)* **410**, 63 (2001).
- [36] G. Joshi, C. G. S. Pillai, P. Raj, and S. K. Malik, Magnetization studies on superconducting  $\text{MgB}_2$ — lower and upper critical fields and critical current density, *Solid. State Commun.* **118**, 445 (2001).
- [37] D. K. Finnemore, J. E. Ostenson, S. L. Bud'ko, G. Lapertot, and P. C. Canfield, Thermodynamic and transport properties of superconducting  $\text{Mg}^{10}\text{B}_2$ , *Phys. Rev. Lett.* **86**, 2420 (2001).
- [38] Y. Takano, H. Takeya, H. Fujii, H. Kumakura, T. Hatano, K. Togano, H. Kito, and H. Ihara, Superconducting properties of  $\text{MgB}_2$  bulk materials prepared by high-pressure sintering, *Appl. Phys. Lett.* **78**, 2914 (2001).
- [39] M. Xu, H. Kitazawa, Y. Takano, J. Ye, K. Nishida, H. Abe, A. Matsushita, N. Tsujii, and G. Kido, Anisotropy of superconductivity from  $\text{MgB}_2$  single crystals, *Appl. Phys. Lett.* **79**, 2779 (2001).
- [40] Y. Machida, S. Sasaki, H. Fujii, M. Furuyama, I. Kakeya, and K. Kadowaki, Ambient-pressure synthesis of single-crystal  $\text{MgB}_2$  and their superconducting anisotropy, *Phys. Rev. B* **67**, 094507 (2003).



- [41] M. Zehetmayer, M. Eisterer, J. Jun, S. M. Kazakov, J. Karpinski, A. Wisniewski, and H. W. Weber, Mixed-state properties of superconducting  $\text{MgB}_2$  single crystals, *Phys. Rev. B* **66**, 052505 (2002).
- [42] H.-J. Kim, B. Kang, M.-S. Park, K.-H. Kim, H. S. Lee, and S.-I. Lee, Reversible magnetization measurement of the anisotropy of the London penetration depth in  $\text{MgB}_2$  single crystals, *Phys. Rev. B* **69**, 184514 (2004).
- [43] B. Kang, H.-J. Kim, M.-S. Park, K.-H. Kim, and S.-I. Lee, Reversible magnetization of  $\text{MgB}_2$  single crystals with a two-gap nature, *Phys. Rev. B* **69**, 144514 (2004).
- [44] Yu. Eltsev, K. Nakao, S. Lee, T. Masui, N. Chikumoto, S. Tajima, N. Koshizuka, and M. Murakami, Anisotropic resistivity and Hall effect in  $\text{MgB}_2$  single crystals, *Phys. Rev. B* **66**, 180504(R) (2002).
- [45] B. Ropers, R. Canet, F. Carmona, and S. Flandrois, Transport properties and percolating behaviour of  $\text{YBaCuO}/\text{Ag}$  random composites above and below  $T_c$ , *Solid State Commun.* **75**, 791 (1990).
- [46] S. Bose and P. Ayyub, Superconducting proximity effect in  $\text{Pb}/\text{Ag}$  nanocomposites, *Phys. Rev. B* **76**, 144510 (2007).
- [47] A. Serquis, X. Z. Liao, Y. T. Zhu, J. Y. Coulter, J. Y. Huang, J. O. Willis, D. E. Peterson, F. M. Mueller, N. O. Moreno, J. D. Thompson, V. F. Nesterenko, and S. S. Indrakanti, Influence of microstructures and crystalline defects on the superconductivity of  $\text{MgB}_2$ , *J. Appl. Phys.* **92**, 351 (2002).
- [48] V. Metlushko, U. Welp, A. Koshelev, I. Aranson, G. W. Crabtree, and P. C. Canfield, Anisotropic upper critical field of  $\text{LuNi}_2\text{B}_2\text{C}$ , *Phys. Rev. Lett.* **79**, 1738 (1997).
- [49] K. D. D. Rathnayaka, A. K. Bhatnagar, A. Parasiris, D. G. Naugle, P. C. Canfield, and B. K. Cho, Transport and superconducting properties of  $\text{RNi}_2\text{B}_2\text{C}$  ( $R = \text{Y}, \text{Lu}$ ) single crystals, *Phys. Rev. B* **55**, 8506 (1997).
- [50] S. V. Shulga, S.-L. Drechsler, G. Fuchs, K.-H. Müller, K. Winzer, M. Heinecke, and K. Krug, Upper critical field peculiarities of superconducting  $\text{YNi}_2\text{B}_2\text{C}$  and  $\text{LuNi}_2\text{B}_2\text{C}$ , *Phys. Rev. Lett.* **80**, 1730 (1998).
- [51] J. Freudenberger, S.-L. Drechsler, G. Fuchs, A. Kreyssig, K. Nenkov, S. V. Shulga, K.-H. Müller, and L. Schultz, Superconductivity and disorder in  $\text{Y}_x\text{Lu}_{1-x}\text{Ni}_2\text{B}_2\text{C}$ , *Physica C* **306**, 1 (1998).
- [52] G. Fuchs, K.-H. Müller, A. Handstein, K. Nenkov, V. N. Narozhnyi, D. Eckert, M. Wolf, and L. Schultz, Upper critical field and irreversibility line in superconducting  $\text{MgB}_2$ , *Solid State Commun.* **118**, 497 (2001).
- [53] W. N. Kang, C. U. Jung, K. H. P. Kim, M.-S. Park, S. Y. Lee, H.-J. Kim, E.-M. Choi, K. H. Kim, M.-S. Kim, and S.-I. Lee, Hole carrier in  $\text{MgB}_2$  characterized by Hall measurements, *Appl. Phys. Lett.* **79**, 982 (2001).
- [54] K. P. McKenna and J. Blumberger, Crossover from incoherent to coherent electron tunneling between defects in  $\text{MgO}$ , *Phys. Rev. B* **86**, 245110 (2012).
- [55] D. C. Larbalestier, L. D. Cooley, M. O. Rikel, A. A. Polyanskii, J. Jiang, S. Patnaik, X. Y. Cai, D. M. Feldmann, A. Gurevich, A. A. Squitieri, M. T. Naus, C. B. Eom, E. E. Hellstrom, R. J. Cava, K. A. Regan, N. Rogado, M. A. Hayward, T. He, J. S. Slusky, P. Khalifah, K. Inumaru, and M. Haas, Strongly linked current flow in polycrystalline forms of the superconductor  $\text{MgB}_2$ , *Nature (London)* **410**, 186 (2001).
- [56] C. P. Bean, Magnetization of high-field superconductors, *Rev. Mod. Phys.* **36**, 31 (1964).
- [57] A. Sugimoto, T. Yamaguchi, and I. Iguchi, Supercurrent distribution in high- $T_c$  superconducting  $\text{YBa}_2\text{Cu}_3\text{O}_{7-y}$  thin films by scanning superconducting quantum interference device microscopy, *Appl. Phys. Lett.* **77**, 3069 (2000).
- [58] F. S. Wells, A. V. Pan, X. R. Wang, S. A. Fedoseev, and H. Hilgenkamp, Analysis of low-field isotropic vortex glass containing vortex groups in  $\text{YBa}_2\text{Cu}_3\text{O}_{7-x}$  thin films visualized by scanning SQUID microscopy, *Sci. Rep.* **5**, 8677 (2015).
- [59] M. Eisterer, M. Zehetmayer, and H. W. Weber, Current percolation and anisotropy in polycrystalline  $\text{MgB}_2$ , *Phys. Rev. Lett.* **90**, 247002 (2003).
- [60] J. Chen, V. Ferrando, P. Orgiani, A. V. Pogrebnyakov, R. H. T. Wilke, J. B. Betts, C. H. Mielke, J. M. Redwing, X. X. Xi, and Qi Li, Enhancement of flux pinning and high-field critical current density in carbon-alloyed  $\text{MgB}_2$  thin films, *Phys. Rev. B* **74**, 174511 (2006).
- [61] D. Dew-Hughes, Flux pinning mechanisms in type-II superconductors, *Philos. Mag.* **30**, 293 (1974).
- [62] P. P. S. Bhadauria, A. Gupta, H. Kishan, and A. V. Narlikar, Effect of excess Mg and nano-additives on the superconducting properties of weakly connected bulk  $\text{MgB}_2$ , *J. Appl. Phys.* **113**, 063908 (2013).
- [63] A. V. Pogrebnyakov, X. X. Xi, J. M. Redwing, V. Vaithyanathan, D. G. Schlom, A. Soukiasian, S. B. Mi, C. L. Jia, J. E. Giencke, C. B. Eom, J. Chen, Y. F. Hu, Y. Cui, and Qi Li, Properties of  $\text{MgB}_2$  thin films with carbon doping, *Appl. Phys. Lett.* **85**, 2017 (2004).
- [64] Y. J. Uemura, L. P. Le, G. M. Luke, B. J. Sternlieb, W. D. Wu, J. H. Brewer, T. M. Riseman, C. L. Seaman, M. B. Maple, M. Ishikawa, D. G. Hinks, J. D. Jorgensen, G. Saito, and H. Yamochi, Basic similarities among cuprate, bismuthate, organic, Chevrel-phase, and heavy-fermion superconductors shown by penetration-depth measurements, *Phys. Rev. Lett.* **66**, 2665 (1991); Erratum: Basic similarities among cuprate, bismuthate, organic, Chevrel-phase, and heavy-fermion superconductors shown by penetration-depth measurement, **68**, 2712(E) (1992).
- [65] V. J. Emery and S. A. Kivelson, Importance of phase fluctuations in superconductors with small superfluid density, *Nature (London)* **374**, 434 (1995).
- [66] L. Merchant, J. Ostrick, R. P. Barber, Jr., and R. C. Dynes, Crossover from phase fluctuation to amplitude-dominated superconductivity: A model system, *Phys. Rev. B* **63**, 134508 (2001).
- [67] O. Simard, C.-D. Hébert, A. Foley, D. Sénéchal, and A.-M. S. Tremblay, Superfluid stiffness in cuprates: Effect of Mott transition and phase competition, *Phys. Rev. B* **100**, 094506 (2019).
- [68] S. Mallik, G. C. Ménard, G. Saiz, H. Witt, J. Lesueur, A. Gloter, L. Benfatto, M. Bibes, and N. Bergeal, Superfluid stiffness of a  $\text{KTaO}_3$ -based two-dimensional electron gas, *Nat. Commun.* **13**, 4625 (2022).
- [69] M. N. Gastiasoro and B. M. Andersen, Enhancing superconductivity by disorder, *Phys. Rev. B* **98**, 184510 (2018).
- [70] V. D. Neverov, A. E. Lukyanov, A. V. Krasavin, A. Vagov, and M. D. Croitoru, Correlated disorder as a way towards robust superconductivity, *Commun. Phys.* **5**, 177 (2022).

- [71] M. Fratini, N. Poccia, A. Ricci, G. Campi, M. Burghammer, G. Aeppli, and A. Bianconi, Scale-free structural organization of oxygen interstitials in  $\text{La}_2\text{CuO}_{4+y}$ , *Nature (London)* **466**, 841 (2010).
- [72] B. Phillabaum, E. W. Carlson, and K. A. Dahmen, Spatial complexity due to bulk electronic nematicity in a superconducting underdoped cuprate, *Nat. Commun.* **3**, 915 (2012).
- [73] M. V. Feigel'man, L. B. Ioffe, V. E. Kravtsov, and E. Cuevas, Fractal superconductivity near localization threshold, *Ann. Phys.* **325**, 1390 (2010).
- [74] C. Rubio-Verdú, A. M. García-García, H. Ryu, D.-J. Choi, J. Zaldívar, S. Tang, B. Fan, Z.-X. Shen, S.-K. Mo, J. I. Pascual, and M. M. Ugeda, Visualization of multifractal superconductivity in a two-dimensional transition metal dichalcogenide in the weak-disorder regime, *Nano Lett.* **20**, 5111 (2020).
- [75] K. Zhao, H. Lin, X. Xiao, W. Huang, W. Yao, M. Yan, Y. Xing, Q. Zhang, Z.-X. Li, S. Hoshino, J. Wang, S. Zhou, L. Gu, M. S. Bahramy, H. Yao, N. Nagaosa, Q.-K. Xue, K. T. Law, X. Chen, and S.-H. Ji, Disorder-induced multifractal superconductivity in monolayer niobium dichalcogenides, *Nat. Phys.* **15**, 904 (2019).
- [76] F. C. Santos and J. M. Pacheco, Scale-free networks provide a unifying framework for the emergence of cooperation, *Phys. Rev. Lett.* **95**, 098104 (2005).
- [77] C. Song, S. Havlin, and H. A. Makse, Origins of fractality in the growth of complex networks, *Nat. Phys.* **2**, 275 (2006).
- [78] J. Martinek and J. Stankowski, Periodic microwave absorption in superconductors, *Phys. Rev. B* **50**, 3995 (1994).
- [79] L. M. Xie, J. Wosik, and J. C. Wolfe, Nonlinear microwave absorption in weak-link Josephson junctions, *Phys. Rev. B* **54**, 15494 (1996).